

# Curvature Regularized Surface Reconstruction from Point Cloud

Yuchen He\*

Sung Ha Kang<sup>†</sup>Hao Liu<sup>‡</sup>

May 5, 2022

## Abstract

We propose a variational functional and fast algorithms to reconstruct implicit surface from point cloud data with a curvature constraint. The minimizing functional balances the distance function from the point cloud and the mean curvature term. Only the point location is used, without any local normal or curvature estimation at each point. With the added curvature constraint, the computation becomes particularly challenging. To enhance the computational efficiency, we solve the problem by a novel operator splitting scheme. It replaces the original high-order PDEs by a decoupled PDE system, which is solved by a semi-implicit method. We also discuss approach using an augmented Lagrangian method. The proposed method shows robustness against noise, and recovers concave features and sharp corners better compared to models without curvature constraint. Numerical experiments in two and three dimensional data sets, noisy and sparse data are presented to validate the model.

## 1 Introduction

In various industrial applications and scientific fields [11, 16], surface reconstruction from point cloud data is a critical step towards informative data visualization and successful high-level processing. Effective methods to reconstruct a continuous surface from finitely many points can help lighten the burden of data transmission and facilitate shape manipulations. One of the main goal of surface reconstruction is to render meaningful and reliable surfaces which naturally captures the geometrical features of the point cloud. We use the celebrated level set function [24] to represent the surface. For  $d \in \mathbb{N}$ , a  $d$ -dimensional implicit surface is represented by the set

$$\Gamma = \{x \in \mathbb{R}^{d+1} \mid \phi(x) = 0\}$$

for a level set function  $\phi : \mathbb{R}^{d+1} \rightarrow \mathbb{R}$ . Implicit surfaces enjoy the flexibility in topological changes, and can easily incorporate geometric features based on  $\phi$ , such as normals, mean curvature, and Gaussian curvature.

Interpreting the reconstructed surface as an elastic membrane attached to the given point cloud, in [38, 39], the authors propose the minimal surface model, which finds 0-level set surface  $\Gamma$  that minimizes the following energy:

$$E_s(\Gamma) = \left( \int_{\Gamma} d^s(\mathbf{x}) d\sigma \right)^{\frac{1}{s}} = \left( \int_{\Omega} d^s(\mathbf{x}) |\nabla \phi(\mathbf{x})| \delta(\phi(x)) d\mathbf{x} \right)^{\frac{1}{s}}. \quad (1)$$

---

\*School of Mathematics, Georgia Institute of Technology, 686 Cherry Street, Atlanta, GA 30332-0160, USA.  
Email: [yhe306@gatech.edu](mailto:yhe306@gatech.edu)

<sup>†</sup>School of Mathematics, Georgia Institute of Technology, 686 Cherry Street, Atlanta, GA 30332-0160, USA.  
Email: [kang@math.gatech.edu](mailto:kang@math.gatech.edu)

<sup>‡</sup>School of Mathematics, Georgia Institute of Technology, 686 Cherry Street, Atlanta, GA 30332-0160, USA.  
Email: [hao.liu@math.gatech.edu](mailto:hao.liu@math.gatech.edu)

Here,  $d\sigma$  is the area element,  $s > 0$  is an exponent coefficient,  $d(\mathbf{x}) = \inf_{\mathbf{y} \in \mathcal{D}} \{|\mathbf{x} - \mathbf{y}|\}$  measures the point-to-surface distance, and  $\mathcal{D}$  is the set of point cloud data. The energy (1) minimizes the surface area and the distance from surface to point cloud. This model (1) is simple, yet effective, and we build our functional based on this model.

Various related approaches are explored based on implicit surface reconstruction: a data-driven logarithmic prior for noisy data is considered in [30], surface tension to enrich the Euler-Lagrange equations in [14], and principal component analysis to reconstruct curves embedded in sub-manifolds in [20]. In [38], convexified image segmentation model with fast algorithm is proposed for implicit surface reconstruction for point clouds. In [7], efficient algorithm for level set method to preserve distance function is proposed. In [19], the authors proposed a variational model consisting of the distance, the normal direction, and the smoothness terms. In [18], the authors defined the surface via a collection of anisotropic Gaussians centered at each entry of the input point cloud, and used TVG-L1 model for minimization. A similar strategy addresses an  $\ell_0$  gradient regularization model in [17].

In this paper, we propose a functional with a curvature constraint to explore the improvement over only having the distance minimization. One example of curvature term is the squared mean curvature,  $\kappa^2$ , such as Euler’s elastica minimization model [28]. In addition to image inpainting, it has been applied to denoising [5], segmentation problem [41]. For any closed surface  $\Gamma$  in  $\mathbb{R}^3$ , the bending energy,

$$\int_{\Gamma} \kappa^2 d\sigma,$$

where  $d\sigma$  denotes the surface area element, is a conformal invariant [2], and it has a universal lower bound [35]:  $\int_{\Gamma} \kappa^2 d\sigma \geq 4\pi$ . This encourages shapes to have rounded corners, and gives a good general regularization. The absolute mean curvature  $|\kappa|$ ,  $\int_{\Gamma} |\kappa| d\sigma$  is another example. This regularization can preserve sharp edges and corners in various cases, e.g., denoising [5, 40] and segmentation [1].

In this paper, we consider  $l_1$  and  $l_2$  norms of the mean curvature for comparison. In [29], graph cuts algorithm is explored for a functional with the absolute mean curvature term for surface reconstruction. There are related work using weighted mean curvature [12], principle curvature [25], Gaussian curvature [13], Menger curvature [10], and other high-order geometrical information, e.g., conformal factor [21] and elastic ratio [27].

Optimizing a curvature regularized functional is a non-convex and non-linear problem. There have been various developments such as multigrid method [4], graph-cut algorithm [29], homotopy method [36] and convex relaxation [3, 26] just to name a few. A semi-implicit scheme is introduced in [31] to simulate the curvature and surface diffusion motion of the interface. One of the major class of methods is based on *splitting* [8]. The common spirit of these methods casts the complicated primal problem into a series of more tamable subproblems, and the minimizer is found using alternative direction method. There are various strategies to obtain such decompositions from the optimization problem. For example, one can derive the associated Euler-Lagrange equations, then apply operator splitting methods on the differential equations, e.g., Lie-Trotter [34]. Recently, a new operator splitting algorithm is proposed for Euler Elastica Model for image smoothing in [5]. One can also introduce auxiliary variables and transform the primal problem into a constrained one, then obtain a series of subproblems by alternatively optimizing one variable at a time while keeping the others fixed; e.g., augmented Lagrangian method (ALM) [1, 32, 33, 37].

We propose surface reconstruction from point cloud with curvature constraint, and explore fast algorithms solving the associated non-convex, non-linear optimization problem. Without prior knowledge about the topology or shape class, our proposed model deforms an implicit surface minimizing Euclidean distance from the point cloud and global curvature-based regularization. We show that the curvature term improves imposing corner features and recovering non-convex parts of the underlying truth. To avoid dealing with the high-order PDEs resulting

from the gradient descent approach, we introduce a semi-implicit method to solve an easier, but equivalent problem derived using operator splitting method (OSM). We also explore an ALM method recently proposed by Bae et al. [1], which reduces the number of parameters compared to other curvature regularized models. Our approaches work effectively in 2D/3D cases, as well as on noisy and sparse point cloud. The contribution of this paper are as follows:

1. We propose a new minimal surface model with curvature-based regularization, and develop fast and efficient algorithms. It is based on OSM form solved by a semi-implicit approach. We also explore an ALM algorithm and discuss the effects of the parameters involved.
2. We explore and numerically compare results using  $l_1$  and  $l_2$  norms of the mean curvature in the functional. We compare using OSM approach and ALM approach.

This paper is organized as follows. In Section 2, we introduce our curvature regularized minimal surface model, and present fast algorithms for the proposed model. In Section 2.1, we introduce a new operator splitting scheme. This approach transforms the original high-order PDE into an easier differential system, which is solved by a semi-implicit method. In Section 2.2, we describe an ALM solution for the model, followed by the numerical details in Section 2.3. Various numerical experiments are presented in Section 3, and analytical discussion is presented in Section 4. We conclude this paper in Section 5.

## 2 Curvature Regularized Surface Reconstruction Model

Let  $\mathcal{D}$  be the set of given point cloud data,  $d(\mathbf{x}) = \inf_{\mathbf{y} \in \mathcal{D}} \{|\mathbf{x} - \mathbf{y}|\}$  measures the point-to-surface distance, and  $d\sigma$  is the area element. To reconstruct a surface from a given point cloud data  $\mathcal{D}$ , we propose the following, curvature constraint minimal surface energy:

$$E_s(\Gamma) = \left( \int_{\Gamma} |d(\mathbf{x})|^s d\sigma \right)^{\frac{1}{s}} + \eta \left( \int_{\Gamma} |\kappa(\mathbf{x})|^s d\sigma \right)^{\frac{1}{s}}. \quad (2)$$

Here,  $\kappa$  is the mean curvature of  $\Gamma$ , and the exponent coefficient  $s > 0$  is a constant integer,  $s = 1$  or  $2$ . The first term, the integral of the distance from point cloud to the surface along the surface, is the fidelity term. It moves the surface  $\Gamma$  closer toward the point cloud. The second term which is the integral of the surface mean curvature along the reconstructed surface is the regularization. This induces regularized geometric features for  $\Gamma$ , independent to the point cloud location. Geometric features can include sharpened corners, smoothed corners, or straightened curve segments, depending on the choice of  $s$ . The parameter  $\eta > 0$  controls the influence of the curvature regularization. When  $\eta = 0$ , the model (2) degenerates to the minimal surface model in [38].

We employ implicit surface representation of the surface [23], and the level set function is defined such that  $\Gamma$  is its zero level set:

$$\phi(\mathbf{x}) \text{ is } \begin{cases} > 0, & \text{if } \mathbf{x} \text{ is outside of } \Gamma, \\ = 0, & \text{if } \mathbf{x} \text{ is on } \Gamma, \\ < 0, & \text{if } \mathbf{x} \text{ is inside } \Gamma. \end{cases}$$

By using  $\phi$ , the functional  $E_s(\Gamma)$  restricted on the surface  $\Gamma$  can be expressed by  $E_s(\phi)$  which is expressed on the domain  $\Omega$ :

$$E_s(\phi) = \left( \int_{\Omega} |d(\mathbf{x})|^s \delta(\phi) |\nabla \phi| d\mathbf{x} \right)^{\frac{1}{s}} + \eta \left( \int_{\Omega} |\kappa(\mathbf{x})|^s \delta(\phi) |\nabla \phi| d\mathbf{x} \right)^{\frac{1}{s}},$$

where  $\delta(\phi) = H'(\phi)$  is the Dirac Delta function with  $H$  being the Heaviside step function:  $H(\phi) = 1$  if  $\phi > 0$ , and 0 otherwise. We use the smoothed approximation [1] for practical computation

$$H_\varepsilon(\phi) = \frac{1}{2} + \frac{1}{\pi} \arctan\left(\frac{\phi}{\varepsilon}\right) \quad \text{and} \quad \delta_\varepsilon(\phi) = H'_\varepsilon(\phi) = \frac{\varepsilon}{\pi(\varepsilon^2 + \phi^2)} \quad (3)$$

with  $\varepsilon > 0$ , which is a constant controlling the smoothness. For any point  $\mathbf{x}$  on  $\Gamma$ , its mean curvature can be computed as,  $\kappa(\mathbf{x}) = \nabla \cdot \left( \frac{\nabla \phi(\mathbf{x})}{|\nabla \phi(\mathbf{x})|} \right)$ . Putting these together, we solve the following smoothed energy:

$$E_{s,\varepsilon}(\phi) = \left( \int_{\Omega} |d(\mathbf{x})|^s \frac{\varepsilon}{\pi(\varepsilon^2 + \phi^2)} |\nabla \phi| d\mathbf{x} \right)^{\frac{1}{s}} + \eta \left( \int_{\Omega} \left| \nabla \cdot \left( \frac{\nabla \phi}{|\nabla \phi|} \right) \right|^s \frac{\varepsilon}{\pi(\varepsilon^2 + \phi^2)} |\nabla \phi| d\mathbf{x} \right)^{\frac{1}{s}}, \quad (4)$$

and the reconstructed surface is defined as the minimizer of the energy (4), i.e.,

$$\Gamma = \{\mathbf{x} | \psi(\mathbf{x}) = 0\} \quad \text{for} \quad \psi = \arg \min_{\phi} E_\varepsilon(\phi).$$

Here  $\psi$  represents the optimal level set function.

## 2.1 Operator Splitting Method

One of the main challenge is that  $E_{s,\varepsilon}$  in (4) is highly nonlinear in terms of  $\phi$  and the corresponding Euler-Lagrange equation is a high-order nonlinear PDE. (It is the combination of equations in (29) and (30) in Section 4 expressed in terms of  $\phi$ .) We propose a new operator splitting strategy to bypass this difficulty, which leads to an equivalent differential equation system that is much easier to solve.

We follow the direction of gradient flow; however, we first decouple the data fidelity term and the curvature regularization term, then minimize the simplified functional via its gradient flow. For  $s = 2$ , using (4), we rewrite the energy (2) in the following equivalent form:

$$\begin{cases} \tilde{E}_{2,\varepsilon}(\phi) = \left( \int_{\Omega} d(\mathbf{x})^2 \delta_\varepsilon(\phi) |\nabla \phi| d\mathbf{x} \right)^{\frac{1}{2}} + \eta \left( \int_{\Omega} q^2 \delta_\varepsilon(\phi) |\nabla \phi| d\mathbf{x} \right)^{\frac{1}{2}}, \\ \text{with } q = \nabla \cdot \frac{\nabla \phi}{|\nabla \phi|}, \end{cases} \quad (5)$$

the notation  $\delta_\varepsilon(\phi)$  as in (3). We then compute the variation of  $\tilde{E}_{2,\varepsilon}(\phi)$  with respect to  $\phi$  [38]. For  $\forall v \in H^1$ ,  $H^1$  denotes the Sobolev space, we have

$$\begin{aligned} \left\langle \frac{\partial \tilde{E}_{2,\varepsilon}(\phi)}{\partial \phi}, v \right\rangle &= \int_{\Omega} \frac{1}{2} \delta_\varepsilon(\phi) \left[ \int_{\Omega} d^2(\mathbf{x}) \delta_\varepsilon(\phi) |\nabla \phi| d\mathbf{x} \right]^{-1/2} \nabla \cdot \left[ d^2(\mathbf{x}) \frac{\nabla \phi}{|\nabla \phi|} \right] v d\mathbf{x} \\ &+ \eta \int_{\Omega} \frac{1}{2} \delta_\varepsilon(\phi) \left[ \int_{\Omega} q^2(\mathbf{x}) \delta_\varepsilon(\phi) |\nabla \phi| d\mathbf{x} \right]^{-1/2} \nabla \cdot \left[ q^2(\mathbf{x}) \frac{\nabla \phi}{|\nabla \phi|} \right] v d\mathbf{x}. \end{aligned}$$

If  $\psi$  is a minimizer of  $\tilde{E}_{2,\varepsilon}$ , it satisfies

$$\left\langle \frac{\partial \tilde{E}_{2,\varepsilon}(\psi)}{\partial \phi}, v \right\rangle = 0, \quad q - \nabla \cdot \frac{\nabla \psi}{|\nabla \psi|} = 0, \quad \forall v \in H^1. \quad (6)$$

To solve for  $\psi$ , we associate (6) with the following initial value problem

$$\begin{cases} \frac{\partial \phi}{\partial t} = f(d, \phi) \nabla \cdot \left[ d^2(\mathbf{x}) \frac{\nabla \phi}{|\nabla \phi|} \right] + \eta f(q, \phi) \nabla \cdot \left[ q^2(\mathbf{x}) \frac{\nabla \phi}{|\nabla \phi|} \right], \\ \frac{\partial q}{\partial t} + \gamma \left( q - \nabla \cdot \frac{\nabla \phi}{|\nabla \phi|} \right) = 0, \end{cases} \quad (7)$$

with

$$f(d, \phi) = \frac{1}{2} \delta_\varepsilon(\phi) \left[ \int_{\Omega} d^2(\mathbf{x}) \delta_\varepsilon(\phi) |\nabla \phi| d\mathbf{x} \right]^{-1/2}.$$

The steady state of (7) is a minimizer of  $\tilde{E}_{2,\varepsilon}$  in (5). On the right hand side of the first equation in (7), the two terms are of the same form, only differ by  $\eta$ ,  $d$  and  $q$ . The first term is the driving velocity to minimize the squared distance to the given data. The second term is the driving velocity to minimize the squared curvature along the reconstructed surface. The parameter  $\eta$  controls the tradeoff between the two terms.

We adopt the Lie type of operator splitting, and refer the reader to [9] for a complete discussion of different splitting schemes. Given  $\{\phi^n, q^n\}$ , we update  $\{\phi^{n+1}, q^{n+1}\}$  in two fractional steps. In particular, for  $k > 0$ , we update the variables through  $\{\phi^k, q^k\} \rightarrow \{\phi^{k+1/2}, q^{k+1/2}\} \rightarrow \{\phi^{k+1}, q^{k+1}\}$  as follows:

Fractional step 1: Solve

$$\begin{cases} \frac{\partial \phi}{\partial t} = f(d, \phi) \nabla \cdot \left[ d^2(\mathbf{x}) \frac{\nabla \phi}{|\nabla \phi|} \right] + \eta f(q, \phi) \nabla \cdot \left[ q^2(\mathbf{x}) \frac{\nabla \phi}{|\nabla \phi|} \right] & \text{on } \Omega \times [t^k, t^{k+1}], \\ \frac{\partial q}{\partial t} = 0 & \text{on } \Omega \times [t^k, t^{k+1}], \\ \phi(t^k) = \phi^k, q(t^k) = q^k \end{cases} \quad (8)$$

and set  $\phi^{k+1/2} = \phi(t^{k+1}), q^{k+1/2} = q(t^{k+1})$ .

Fractional step 2: Solve

$$\begin{cases} \frac{\partial \phi}{\partial t} = 0 & \text{on } \Omega \times [t^k, t^{k+1}], \\ \frac{\partial q}{\partial t} + \gamma(q - \nabla \cdot \frac{\nabla \phi^{k+1/2}}{|\nabla \phi^{k+1/2}|}) = 0 & \text{on } \Omega \times [t^k, t^{k+1}], \\ \phi(t^k) = \phi^{k+1/2}, q(t^k) = q^{k+1/2} \end{cases} \quad (9)$$

and set  $\phi^{k+1} = \phi(t^{k+1}), q^{k+1} = q(t^{k+1})$ .

We have two subproblems (8) and (9) to solve. There is no difficulty to solve (9), since we have the closed form solution:

$$q = e^{\gamma \Delta t} q^{k+1/2} + (1 - e^{\gamma \Delta t}) \nabla \cdot \frac{\nabla \phi^{k+1/2}}{|\nabla \phi^{k+1/2}|}.$$

To solve (8) for  $\phi^{k+1/2}$ , the simplest way is to use the explicit scheme as the following:

$$\frac{\phi^{k+1/2} - \phi^k}{\Delta t} = f(d, \phi^k) \nabla \cdot \left[ d^2(\mathbf{x}) \frac{\nabla \phi^k}{|\nabla \phi^k|} \right] + \eta f(q^k, \phi^k) \nabla \cdot \left[ (q^k)^2(\mathbf{x}) \frac{\nabla \phi^k}{|\nabla \phi^k|} \right].$$

However, due to the stability consideration, one needs to choose a very small time step of order  $O(h^2)$  where  $h$  is the spacial step size. To relax the time step constraint, we add  $-\alpha \Delta \phi$  on both sides of (8), as in [31], to get

$$\frac{\partial \phi}{\partial t} - \alpha \Delta \phi = -\alpha \Delta \phi + f(d, \phi) \nabla \cdot \left[ d^2(\mathbf{x}) \frac{\nabla \phi}{|\nabla \phi|} \right] + \eta f(q, \phi) \nabla \cdot \left[ q^2(\mathbf{x}) \frac{\nabla \phi}{|\nabla \phi|} \right]. \quad (10)$$

We discretize (10) in time semi-implicitly:

$$\frac{\phi^{k+1/2} - \phi^k}{\Delta t} - \alpha \Delta \phi^{k+1/2} = -\alpha \Delta \phi^k + f(d, \phi^k) \nabla \cdot \left[ d^2(\mathbf{x}) \frac{\nabla \phi^k}{|\nabla \phi^k|} \right] + \eta f(q^k, \phi^k) \nabla \cdot \left[ (q^k)^2(\mathbf{x}) \frac{\nabla \phi^k}{|\nabla \phi^k|} \right].$$

We choose  $\alpha = 1$ . This equation is a Laplacian equation of  $\phi^{k+1/2}$  and can be solved efficiently by fast Fourier transformation (FFT). The updating formula can be summarized as

$$\begin{cases} \frac{\phi^{k+1} - \phi^k}{\Delta t} - \alpha \Delta \phi^{k+1} = -\alpha \Delta \phi^n + f(d, \phi^k) \nabla \cdot \left[ d^2(\mathbf{x}) \frac{\nabla \phi^k}{|\nabla \phi^k|} \right] + \eta f(q^k, \phi^k) \nabla \cdot \left[ (q^k)^2(\mathbf{x}) \frac{\nabla \phi^k}{|\nabla \phi^k|} \right], \\ q^{k+1} = e^{\gamma \Delta t} q^k + (1 - e^{\gamma \Delta t}) \nabla \cdot \frac{\nabla \phi^{k+1}}{|\nabla \phi^{k+1}|}. \end{cases} \quad (11)$$

To solve (11), we need the initial condition  $(\phi^0, q^0)$ . We choose  $\phi^0$  to be a signed distance function whose zero level set encloses all data.  $q^0$  is assigned as  $\nabla \cdot ((\nabla \phi^0)/|\nabla \phi^0|)$ . The algorithm of OSM with  $s = 2$  is stated in Algorithm 1.

---

**Algorithm 1:** Operator Splitting Method (OSM) for  $s = 2$ .

---

**Initialization:**  $d, \phi^0, q^0$ .

**while** *not converge* **do**

    | Update  $\{\phi^{k+1}, q^{k+1}\}$  by solving (11).

**end**

**Output:**  $\phi^k$ .

---

In the following, we give a brief derivation of OSM for  $s = 1$ . With  $s = 1$ ,  $E_{1,\varepsilon}$  has the same minimizer as

$$\begin{cases} \tilde{E}_{1,\varepsilon}(\phi) = \int_{\Omega} d(\mathbf{x}) \delta_{\varepsilon}(\phi) |\nabla \phi| d\mathbf{x} + \eta \int_{\Omega} |q| \delta_{\varepsilon}(\phi) |\nabla \phi| d\mathbf{x}, \\ \text{with } q = \nabla \cdot \frac{\nabla \phi}{|\nabla \phi|}, \end{cases}$$

whose variation with respect to  $\phi$  is given as

$$\left\langle \frac{\partial \tilde{E}_{1,\varepsilon}(\phi)}{\partial \phi}, v \right\rangle = \nabla \cdot \left[ d(\mathbf{x}) \frac{\nabla \phi}{|\nabla \phi|} \right] v d\mathbf{x} + \eta \nabla \cdot \left[ |q| \frac{\nabla \phi}{|\nabla \phi|} \right] v d\mathbf{x}.$$

The corresponding gradient flow initial value problem is

$$\begin{cases} \frac{\partial \phi}{\partial t} = \nabla \cdot \left[ d(\mathbf{x}) \frac{\nabla \phi}{|\nabla \phi|} \right] + \eta \nabla \cdot \left[ |q| \frac{\nabla \phi}{|\nabla \phi|} \right], \\ \frac{\partial q}{\partial t} + \gamma (q - \nabla \cdot \frac{\nabla \phi}{|\nabla \phi|}) = 0. \end{cases} \quad (12)$$

With the Lie type splitting in time and introducing the term  $-\alpha \Delta \phi$  on both sides in the first equation of (12), the updating formula becomes

$$\begin{cases} \frac{\phi^{k+1} - \phi^k}{\Delta t} - \alpha \Delta \phi^{k+1} = -\alpha \Delta \phi^k + \nabla \cdot \left[ d(\mathbf{x}) \frac{\nabla \phi^k}{|\nabla \phi^k|} \right] + \eta \nabla \cdot \left[ |q^k| \frac{\nabla \phi^k}{|\nabla \phi^k|} \right], \\ q^{k+1} = e^{\gamma \Delta t} q^k + (1 - e^{\gamma \Delta t}) \nabla \cdot \frac{\nabla \phi^{k+1}}{|\nabla \phi^{k+1}|}. \end{cases} \quad (13)$$

## 2.2 Augmented Lagrangian Method

We present another efficient algorithm to find the minimizer of (4) with  $s = 1$ . The reason for only focusing on  $s = 1$  in this case is that we can take advantage of the shrinkage operator. We first introduce three new variables:  $\mathbf{p} = \nabla \phi$ ,  $\mathbf{n} = \nabla \phi / |\nabla \phi|$  and  $q = \nabla \cdot (\nabla \phi / |\nabla \phi|)$ . Finding the minimizer of  $E_{1,\varepsilon}$  becomes equivalent to solving

$$\min_{\phi, \mathbf{p}, \mathbf{n}, q} \int \varepsilon \frac{(d(\mathbf{x}) + \eta |q|) |\mathbf{p}|}{\pi(\varepsilon^2 + \phi^2)} d\mathbf{x} \quad \text{with} \quad \mathbf{p} = \nabla \phi, \quad \mathbf{n} = \nabla \phi / |\nabla \phi|, \quad q = \nabla \cdot (\nabla \phi / |\nabla \phi|).$$

This can be solved via alternating direction method of multipliers by introducing Lagrange multipliers  $\lambda_1, \lambda_2, \lambda_3$ . The associated Augmented Lagrangian functional is

$$\begin{aligned} \mathcal{L}(\phi, q, \mathbf{p}, \mathbf{n}, \lambda_1, \lambda_2, \lambda_3) &= \int_{\Omega} \frac{\varepsilon(d + \eta|q|)|\mathbf{p}|}{\pi(\varepsilon^2 + \phi^2)} dx + \frac{r_1}{2} \int_{\Omega} |\mathbf{p} - \nabla\phi|^2 dx + \int_{\Omega} \lambda_1 \cdot (\mathbf{p} - \nabla\phi) dx \\ &+ \frac{r_2}{2} \int_{\Omega} (q - \nabla \cdot \mathbf{n})^2 dx + \int_{\Omega} \lambda_2 (q - \nabla \cdot \mathbf{n}) dx + \frac{r_3}{2} \int_{\Omega} \|\mathbf{p}\mathbf{n} - \mathbf{p}\|^2 dx + \int_{\Omega} \lambda_3 \cdot (\|\mathbf{p}\mathbf{n} - \mathbf{p}\|) . \end{aligned} \quad (14)$$

where  $\mathbf{p}, \mathbf{n}, \lambda_1, \lambda_3$  are vectors,  $\phi, q, \lambda_2$  are scalars,  $r_1, r_2, r_3$  are fixed constants. To find the saddle point of  $\mathcal{L}$ , we update each variable in an iterative manner. In each iteration, for each variable, we minimize the corresponding functional while keep other variables fixed. After all variables are updated, we update Lagrange multipliers. This procedure is repeated until we achieve the steady state. In each iteration, we have four subproblems to minimize:

$$\mathcal{E}_1(\phi) = \int_{\Omega} \frac{\varepsilon(d + \eta|q|)|\mathbf{p}|}{\pi(\varepsilon^2 + \phi^2)} dx + \frac{r_1}{2} \int_{\Omega} |\mathbf{p} - \nabla\phi|^2 dx + \int_{\Omega} \lambda_1 \cdot (\mathbf{p} - \nabla\phi) dx \quad (15)$$

$$\mathcal{E}_2(q) = \int_{\Omega} \frac{\varepsilon(d + \eta|q|)|\mathbf{p}|}{\pi(\varepsilon^2 + \phi^2)} dx + \frac{r_2}{2} \int_{\Omega} (q - \nabla \cdot \mathbf{n})^2 dx + \int_{\Omega} \lambda_2 (q - \nabla \cdot \mathbf{n}) dx, \quad (16)$$

$$\begin{aligned} \mathcal{E}_3(\mathbf{p}) &= \int_{\Omega} \frac{\varepsilon(d + \eta|q|)|\mathbf{p}|}{\pi(\varepsilon^2 + \phi^2)} dx + \frac{r_1}{2} \int_{\Omega} |\mathbf{p} - \nabla\phi|^2 dx + \int_{\Omega} \lambda_1 \cdot (\mathbf{p} - \nabla\phi) dx, \\ &+ \frac{r_3}{2} \int_{\Omega} \|\mathbf{p}\mathbf{n} - \mathbf{p}\|^2 dx + \int_{\Omega} \lambda_3 \cdot (\|\mathbf{p}\mathbf{n} - \mathbf{p}\|) . \end{aligned} \quad (17)$$

$$\begin{aligned} \mathcal{E}_4(\mathbf{n}) &= \frac{r_2}{2} \int_{\Omega} (q - \nabla \cdot \mathbf{n})^2 dx + \int_{\Omega} \lambda_2 (q - \nabla \cdot \mathbf{n}) dx + \frac{r_3}{2} \int_{\Omega} \|\mathbf{p}\mathbf{n} - \mathbf{p}\|^2 dx \\ &+ \int_{\Omega} \lambda_3 \cdot (\|\mathbf{p}\mathbf{n} - \mathbf{p}\|) . \end{aligned} \quad (18)$$

After those four variables being updated correspondingly, Lagrange multipliers are updated as

$$\lambda_1 \leftarrow \lambda_1 + r_1(\mathbf{p} - \nabla\phi), \quad \lambda_2 \leftarrow \lambda_2 + r_2(q - \nabla \cdot \mathbf{n}), \quad \lambda_3 \leftarrow \lambda_3 + r_3(\|\mathbf{p}\mathbf{n} - \mathbf{p}\|).$$

The four subproblems can be solved efficiently as follows:

Subproblem of  $\phi$ : For  $\mathcal{E}_1(\phi)$  in (15), the corresponding Euler-Lagrange equation is:

$$-r_1 \Delta\phi + \beta\phi = \beta\phi + (g + \eta|q|) \frac{2\varepsilon|\mathbf{p}|\phi}{\pi(\varepsilon^2 + \phi^2)^2} - \nabla \cdot (r_1\mathbf{p} + \lambda_1)$$

where  $\beta > 0$  is a frozen coefficient. We time-discretize as following:

$$-r_1 \Delta\phi^{k+1} + \beta\phi^{k+1} = \beta\phi^k + (g + \eta|q^k|) \frac{2\varepsilon|\mathbf{p}^k|\phi^k}{\pi(\varepsilon^2 + (\phi^k)^2)^2} - \nabla \cdot (r_1\mathbf{p}^k + \lambda_1^k) \quad (19)$$

This is a Laplacian equation of  $\phi^{k+1}$ , and we efficiently solve by FFT.

Subproblem of  $q$ : In (16),  $\mathcal{E}_2(\phi)$  can be written as:

$$\mathcal{E}_2(q) = \int_{\Omega} \frac{\eta\varepsilon|\mathbf{p}|}{\pi(\varepsilon^2 + \phi^2)} |q| + \frac{r_2}{2} (q - (\nabla \cdot \mathbf{n} - \frac{\lambda_2}{r_2}))^2 dx + C$$

where  $C$  is independent of  $q$ . Then, the minimizer can be found via shrinkage operator:

$$\arg \min_q \mathcal{E}_2(q) = \max \left\{ 0, 1 - \frac{\eta\varepsilon|\mathbf{p}|}{r_2\pi(\varepsilon^2 + \phi^2)|q^*|} \right\} q^*, \quad (20)$$

with  $q^* = \nabla \cdot \mathbf{n} - \lambda_2/r_2$ .

Subproblem of  $\mathbf{p}$ : In (17),  $\mathcal{E}_3(\phi)$  can be rewritten as:

$$\begin{aligned} \mathcal{E}_3(\mathbf{p}) = & \int_{\Omega} \underbrace{\left[ (d + \eta|q|) \frac{\varepsilon}{\pi(\varepsilon^2 + \phi^2)} + \boldsymbol{\lambda}_3 \cdot \mathbf{n} \right]}_{\omega} |\mathbf{p}| + \underbrace{\frac{r_1 + r_3(1 + |\mathbf{n}|^2)}{2}}_{\mu} \left| \mathbf{p} - \underbrace{\frac{\boldsymbol{\lambda}_3 + r_1 \nabla \phi - \boldsymbol{\lambda}_1}{r_1 + r_3(1 + |\mathbf{n}|^2)}}_{\mathbf{a}} \right|^2 \\ & - \int_{\Omega} \underbrace{r_3 \mathbf{n}}_{\boldsymbol{\nu}} \cdot \mathbf{p} |\mathbf{p}| + \tilde{C}, \end{aligned}$$

where  $\tilde{C}$  is independent of  $\mathbf{p}$ . This  $\mathcal{E}_3(\mathbf{p})$  can be simplified as

$$\mathcal{E}_3(\mathbf{p}) = \int_{\Omega} \omega |\mathbf{p}| + \mu |\mathbf{p} - \mathbf{a}| - \boldsymbol{\nu} \cdot \mathbf{p} |\mathbf{p}| + \tilde{C}.$$

Following the idea of Theorem 2 in [1], we can design a fast algorithm as follows:

**Theorem 2.1.** Assume that  $\mu > 2|\boldsymbol{\nu}|$ . Let  $\theta$  be the angle between  $\mathbf{a}$  and the minimum vector of  $\mathcal{E}_3(\mathbf{p})$ , and  $\alpha$  is the angle between  $\mathbf{a}$  and  $\boldsymbol{\nu}$ . Then the following arguments hold:

- if  $\omega \geq \mu|\mathbf{a}|$ , then  $\arg \min_{\mathbf{p}} \mathcal{E}_3(\mathbf{p}) = \mathbf{0}$ .
- if  $\omega < \mu|\mathbf{a}|$ :

1. if  $\mathbf{a} = \boldsymbol{\nu} = \mathbf{0}$ , then  $\arg \min_{\mathbf{p}} \mathcal{E}_3(\mathbf{p}) = \begin{cases} \mathbf{0}, & \text{when } \omega \geq 0, \\ \text{any vector of length } -\omega/\mu, & \text{when } \omega < 0; \end{cases}$
2. if  $\mathbf{a} \neq \mathbf{0}, \boldsymbol{\nu} = \mathbf{0}$ ,  $\arg \min_{\mathbf{p}} \mathcal{E}_3(\mathbf{p}) = (1 - \frac{\omega}{\mu|\mathbf{a}|})\mathbf{a}$ ;
3. if  $\mathbf{a} = \mathbf{0}, \boldsymbol{\nu} \neq \mathbf{0}$ ,  $\arg \min_{\mathbf{p}} \mathcal{E}_3(\mathbf{p}) = \frac{\omega}{\mu - 2|\boldsymbol{\nu}|} \frac{\boldsymbol{\nu}}{|\boldsymbol{\nu}|}$ ;
4. if  $\mathbf{a} \neq \mathbf{0}, \boldsymbol{\nu} \neq \mathbf{0}$ , the angles  $\theta$  and  $\alpha$  satisfy the equation:

$$\mu^2 |\mathbf{a}| \sin \theta + \mu |\boldsymbol{\nu}| |\mathbf{a}| \sin \theta \cos(\theta - \alpha) + \omega |\boldsymbol{\nu}| \sin(\theta - \alpha) + \mu |\mathbf{a}| |\boldsymbol{\nu}| \sin \alpha = 0, \quad (21)$$

and  $\arg \min_{\mathbf{p}} \mathcal{E}_3(\mathbf{p}) = \frac{[\mu(\mathbf{b} \cdot \mathbf{a}) - \omega] \mathbf{b}}{\mu + 2\boldsymbol{\nu} \cdot \mathbf{b}}$  with  $\mathbf{b}$  being a unit vector satisfying:

$$\mathbf{b} = \frac{1}{|\mathbf{a}|} \begin{bmatrix} \cos \tilde{\theta} & -\sin \tilde{\theta} \\ \sin \tilde{\theta} & \cos \tilde{\theta} \end{bmatrix} \mathbf{a}$$

and  $\tilde{\theta} = \theta$  if  $\det[\boldsymbol{\nu} \ \mathbf{a}] \geq 0$ ,  $\tilde{\theta} = -\theta$  if  $\det[\boldsymbol{\nu} \ \mathbf{a}] < 0$ . Here  $[\boldsymbol{\nu} \ \mathbf{a}]$  denotes the  $2 \times 2$  matrix with the vector  $\boldsymbol{\nu}$  and  $\mathbf{a}$  being the first and second column respectively.

Note that the condition in Theorem 2.1 is always satisfied since  $\mu = \frac{r_1 + r_3(1 + |\mathbf{n}|^2)}{2}$ ,  $\boldsymbol{\nu} = r_3 \mathbf{n}$  and  $r_3(1 + |\mathbf{n}|^2) \geq 2r_3|\mathbf{n}|$  for any  $\mathbf{n}$ . The equation (21),  $\theta$ , is solved by Newton's method.

Subproblem of  $\mathbf{n}$ . For  $\mathcal{E}_4(\phi)$  in (18), the Euler-Lagrange equation is:

$$-r_2 \nabla(\nabla \cdot \mathbf{n}) + D\mathbf{n} = (D - r_3|\mathbf{p}|^2)\mathbf{n} - \nabla(r_2 q + \lambda_2) - (\boldsymbol{\lambda}_3 - r_3 \mathbf{p})|\mathbf{p}| \quad (22)$$

where  $D = \max_{x \in \Omega} (r_3|\mathbf{p}|^2 + \beta_2)$  and  $\beta_2$  is a small positive number. We discretize in time as

$$-r_2 \nabla(\nabla \cdot \mathbf{n}^{n+1}) + D\mathbf{n}^{n+1} = (D - r_3|\mathbf{p}^n|^2)\mathbf{n}^n - \nabla(r_2 q^n + \lambda_2^n) - (\boldsymbol{\lambda}_3^n - r_3 \mathbf{p}^n)|\mathbf{p}^n|. \quad (23)$$

which can be solved efficiently by FFT.

For the initial condition, we use the same  $\phi^0$  and  $q^0$  as that in OSM. For other variables, we use  $\mathbf{p}^0 = \nabla \phi^0$ ,  $\mathbf{n}^0 = \mathbf{p}^0/|\mathbf{p}^0|$ ,  $\boldsymbol{\lambda}_1^0 = \boldsymbol{\lambda}_3^0 = \mathbf{0}$ ,  $\lambda_2^0 = 0$ .

The outline of augmented Lagrangian is summarized in Algorithm 2.



---

**Algorithm 2:** Augmented Lagrangian Method (ALM) for  $s = 1$ .

---

**Initialization:**  $d, \phi^0, q^0, \mathbf{p}^0, \mathbf{n}^0, \boldsymbol{\lambda}_1^0, \lambda_2^0, \boldsymbol{\lambda}_3^0$ .

**while not converge do**

**Update variables**

    Update  $\phi^{k+1} = \arg \min_{\phi} \mathcal{L}(\phi, q^k, \mathbf{p}^k, \mathbf{n}^k, \boldsymbol{\lambda}_1^k, \lambda_2^k, \boldsymbol{\lambda}_3^k)$  by solving (19).

    Update  $q^{k+1} = \arg \min_q \mathcal{L}(\phi^k, q, \mathbf{p}^k, \mathbf{n}^k, \boldsymbol{\lambda}_1^k, \lambda_2^k, \boldsymbol{\lambda}_3^k)$  by solving (20).

    Update  $\mathbf{p}^{k+1} = \arg \min_{\mathbf{p}} \mathcal{L}(\phi^k, q^k, \mathbf{p}, \mathbf{n}^k, \boldsymbol{\lambda}_1^k, \lambda_2^k, \boldsymbol{\lambda}_3^k)$  according to Theorem 2.1.

    Update  $\mathbf{n}^{k+1} = \arg \min_{\mathbf{n}} \mathcal{L}(\phi^k, q^k, \mathbf{p}^k, \mathbf{n}, \boldsymbol{\lambda}_1^k, \lambda_2^k, \boldsymbol{\lambda}_3^k)$  by solving (23).

**Update Lagrange multipliers:**

$$\boldsymbol{\lambda}_1^{k+1} = \boldsymbol{\lambda}_1^k + r_1(\mathbf{p}^{k+1} - \nabla \phi^{k+1}),$$

$$\lambda_2^{k+1} = \lambda_2^k + r_2(q^{k+1} - \nabla \cdot \mathbf{n}^{k+1}),$$

$$\boldsymbol{\lambda}_3^{k+1} = \boldsymbol{\lambda}_3^k + r_3(\mathbf{n}^{k+1} |\mathbf{p}^{k+1}| - \mathbf{p}^{k+1}).$$

**end**

**Output:**  $\phi^k$ .

---

### 2.3 Numerical Implementation Details

For a rectangular domain  $\Omega = [0, M] \times [0, N] \in \mathbb{R}^2$  with  $M, N$  being positive integers, we discretize it by Cartesian grid with  $\Delta x = \Delta y = 1$ . For any function  $u$  (resp.  $\mathbf{v} = (v^1, v^2)^T$ ) defined on  $\Omega$ , we use  $u_{i,j}$  (resp.  $\mathbf{v}_{i,j} = (v_{i,j}^1, v_{i,j}^2)^T$ ) to denote  $u(i\Delta x, j\Delta y)$  (resp.  $\mathbf{v}(i\Delta x, j\Delta y)^T$ ) for  $0 \leq i \leq M, 0 \leq j \leq N$ . Denote the standard forward and backward difference as

$$\begin{aligned} \partial_1^- u_{i,j} &= \begin{cases} u_{i,j} - u_{i-1,j}, & 1 < i \leq M; \\ u_{1,j} - u_{M,j}, & i = 1. \end{cases} & \partial_1^+ u_{i,j} &= \begin{cases} u_{i+1,j} - u_{i,j}, & 1 \leq i < M-1; \\ u_{1,j} - u_{M,j}, & i = M. \end{cases} \\ \partial_2^- u_{i,j} &= \begin{cases} u_{i,j} - u_{i,j-1}, & 1 < j \leq N; \\ u_{i,1} - u_{i,N}, & j = 1. \end{cases} & \partial_2^+ u_{i,j} &= \begin{cases} u_{i,j+1} - u_{i,j}, & 1 \leq j < N-1; \\ u_{i,1} - u_{i,N}, & j = N. \end{cases} \end{aligned}$$

Then the gradient, divergence and the Laplacian operators are approximated as follows:

$$\begin{aligned} \nabla u_{i,j} &= ((\partial_1^- u_{i,j} + \partial_1^+ u_{i,j})/2, (\partial_2^- u_{i,j} + \partial_2^+ u_{i,j})/2); \\ \nabla \cdot \mathbf{v}_{i,j} &= (\partial_1^+ v_{i,j}^1 + \partial_1^- v_{i,j}^1)/2 + (\partial_2^+ v_{i,j}^2 + \partial_2^- v_{i,j}^2)/2; \\ \Delta u_{i,j} &= \partial_1^+ u_{i,j} - \partial_1^- u_{i,j} + \partial_2^+ u_{i,j} - \partial_2^- u_{i,j}. \end{aligned}$$

Denote discrete Fourier transform and its inverse by  $\mathcal{F}$  and  $\mathcal{F}^{-1}$  respectively. For a function  $u$ , we have

$$\mathcal{F}(u)(i \pm 1, j) = e^{\pm 2\pi\sqrt{-1}(i-1)/M} \mathcal{F}(u)(i, j), \quad \mathcal{F}(u)(i, j \pm 1) = e^{\pm 2\pi\sqrt{-1}(j-1)/N} \mathcal{F}(u)(i, j),$$

which give rise to

$$\mathcal{F}(\partial_1^- u)(i, j) = (1 - e^{-2\pi\sqrt{-1}(i-1)/M}) \mathcal{F}(u)(i, j).$$

$\mathcal{F}(\partial_1^+ u)(i, j)$ ,  $\mathcal{F}(\partial_2^- u)(i, j)$  and  $\mathcal{F}(\partial_2^+ u)(i, j)$  can be computed similarly. Both OS and ALM utilizes FFT. The first equation in (13) and (19) belong to the same class of equation:

$$-a\Delta u + bu = c \tag{24}$$

for a function  $u$  with constants  $a, b > 0$  and constant  $c$ . Using Fourier transform, we have

$$\mathcal{F}(\Delta u)(i, j) = [2 \cos(\pi\sqrt{-1}(i-1)/M) + 2 \cos(\pi\sqrt{-1}(j-1)/N) - 4] \mathcal{F}u(i, j).$$

Then (24) can be solved as

$$u = \mathcal{F}^{-1} \left( \frac{\mathcal{F}(c)}{b - a(2 \cos(\pi\sqrt{-1}(i-1)/M) + 2 \cos(\pi\sqrt{-1}(j-1)/N) - 4)} \right).$$

The equation (22) is in the form of

$$-a\nabla(\nabla \cdot \mathbf{v}) + b\mathbf{v} = \mathbf{c} \quad (25)$$

for some vector valued function  $\mathbf{v} = (v^1, v^2)^T$  where  $a, b$  are constant positive scalars and  $\mathbf{c} = (c^1, c^2)^T$  is vector valued constant. After distretization, (25) can be written as

$$\begin{cases} -a\nabla(\partial_1^+ \partial_1^- v^1 + \partial_1^+ \partial_2^- v^2) + bv^1 = c^1, \\ -a\nabla(\partial_2^+ \partial_1^- v^1 + \partial_2^+ \partial_2^- v^2) + bv^2 = c^2. \end{cases} \quad (26)$$

Apply discrete Fourier transform on both sides, (26) becomes equivalent to

$$A \begin{bmatrix} \mathcal{F}(v^1)(i, j) \\ \mathcal{F}(v^2)(i, j) \end{bmatrix} = \begin{bmatrix} \mathcal{F}(c^1)(i, j) \\ \mathcal{F}(c^2)(i, j) \end{bmatrix} \quad (27)$$

with

$$A = \begin{bmatrix} b - a(e^{\sqrt{-1}(i-1)/M} - 1)(1 - e^{-\sqrt{-1}(i-1)/M}) & -a(e^{\sqrt{-1}(i-1)/M} - 1)(1 - e^{-\sqrt{-1}(j-1)/N}) \\ -a(e^{\sqrt{-1}(j-1)/N} - 1)(1 - e^{-\sqrt{-1}(i-1)/M}) & b - a(e^{\sqrt{-1}(j-1)/N} - 1)(1 - e^{-\sqrt{-1}(j-1)/N}) \end{bmatrix}.$$

Then  $\mathbf{v}$  can be computed by first solving (27) for  $(\mathcal{F}(v^1), \mathcal{F}(v^2))^T$  and then apply inverse Fourier transform.

For any  $\mathbf{x} \in \Omega$ ,  $d(\mathbf{x})$  is the distance from  $\mathbf{x}$  to the collection of the point cloud  $\mathcal{D}$ , and it can be computed by solving the Eikonal equation

$$\begin{cases} |\nabla d| = 1, \\ d(\mathbf{x}) = 0, \quad \forall \mathbf{x} \in \mathcal{D}. \end{cases} \quad (28)$$

The simplest monotonic scheme to discretize (28) is the Lax-Friedrich scheme which leads to the updating formula [15]:

$$d_{i,j}^{n+1} = \frac{1}{2} \left( 1 - |\nabla d_{i,j}^n| + \frac{d_{i+1,j}^n + d_{i-1,j}^n}{2} + \frac{d_{i,j+1}^n + d_{i,j-1}^n}{2} \right).$$

This is updated with a fast sweeping method.

To make our algorithm robust, when updating  $\phi$ , we reinitialize the level set to be the signed distance function via solving

$$\phi_\tau + \text{sign}(\phi)(1 - |\nabla \phi|) = 0.$$

In practice, after each iteration, we only solve this for a few iterations. For three dimensional space, we use simple extension from two dimensional case.

### 3 Numerical Results and Comparisons

We present numerical results of the proposed model (2): without specification, when OSM is used, we refer to Algorithm 1 for model (5) with,  $\gamma = 10, \alpha = 1$  and  $\Delta t = 50$ ; when ALM is used, we refer to Algorithm 2 for model (14) with  $\beta = 0.1$ . For a fixed  $\eta$ , OSM only has one (the time step) parameter, whereas ALM has three parameters  $(r_1, r_2, r_3)$ . We use domain  $[0, 100]^2$  for two dimensional problems and  $[0, 50]^3$  for three dimensional problems. In all examples,  $\varepsilon = 1$  is used.

In this section, we first consider the effect of parameters for ALM. Second, we compare the performance of ALM and OSM. Third, we use OSM with  $s = 2$  and further explore different aspects of the model, since results are the most stable for model (5) with  $s = 2$ .

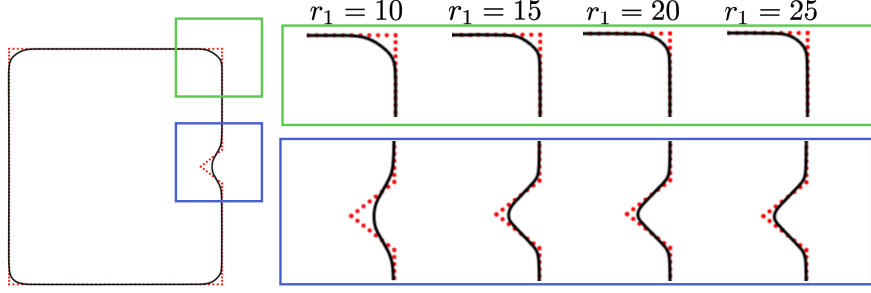


Figure 1: Effect of  $r_1$  in ALM. For fixed  $r_2 = 10$ ,  $r_3 = 3$ , and  $\eta = 2$ , increasing  $r_1$  induces better reconstruction on the concave part.

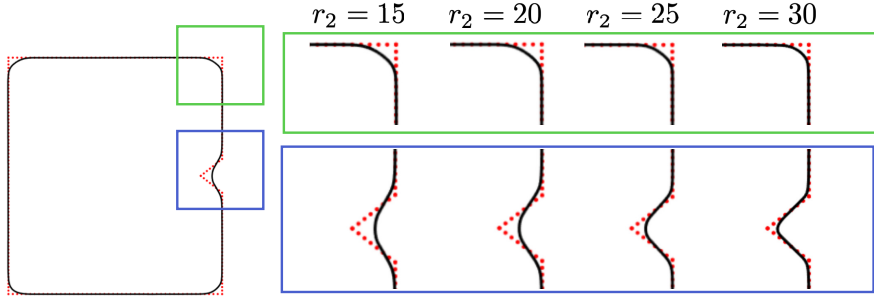


Figure 2: Effect of  $r_2$  in ALM. For fixed  $r_1 = 10$ ,  $r_3 = 3$ , and  $\eta = 2$ , increasing  $r_2$  induces better reconstruction on the concave part.

### 3.1 Choice of Parameters for ALM Method

In the case of ALM, the choice and combinations of the parameters are delicate. When  $r_1$  or  $r_2$  is increased, the reconstruction become closer to the point cloud. In Figure 1, we fix  $r_2 = 10$ ,  $r_3 = 3$ , and  $\eta = 2$ , and let  $r_1$  vary. With increased  $r_1$ , ALM renders the curve closer to the point cloud. In Figure 2, we fix  $r_1 = 10$ ,  $r_3 = 3$ , and  $\eta = 2$ , and let  $r_2$  vary; the larger  $r_2$  induces better reconstruction. For this example,  $r_3$  has a little influence, yet, with a large  $r_3$ , the results may become unstable or divergent.

In Figure 3, we fix  $r_1 = 15$ ,  $r_2 = 10$ , and  $r_3 = 3$ , and increase  $\eta$ . With more influence of curvature, as  $\eta$  is increased from 0 to 1, the indent on the rectangle is better reconstructed. When we increase  $\eta$  from 1 to 5, we see that, the indent is preserved, yet the tip of the wedge does not extend inward as much as in the case where  $\eta = 1$ . This is because large  $\eta$  encourages both small mean curvature and short curve length. We find that increasing  $\eta$  also helps to avoid oscillation during the iteration. In Figure 3, we plot the energy curves corresponding to the three cases mentioned. Before the 100-th step, these curves are indistinguishable; however, after the 100-th step, larger  $\eta$  suppresses the oscillation of the energy curve, leading to a more stable convergence.

Figure 4 shows the robustness against noise. The point cloud is sampled from a circle on  $\Omega = [0, 200]^2$ , and Gaussian noise with standard deviation 2 is added to the data. Using ALM with  $r_1 = 15$ ,  $r_2 = 10$ ,  $r_3 = 3$ ,  $\eta$  is varied from 0, 1, to 10. Figure 4(a) shows similar performances, while the zoomed-in results in Figure 4(b) shows that the larger the  $\eta$  is the smoother the result becomes.

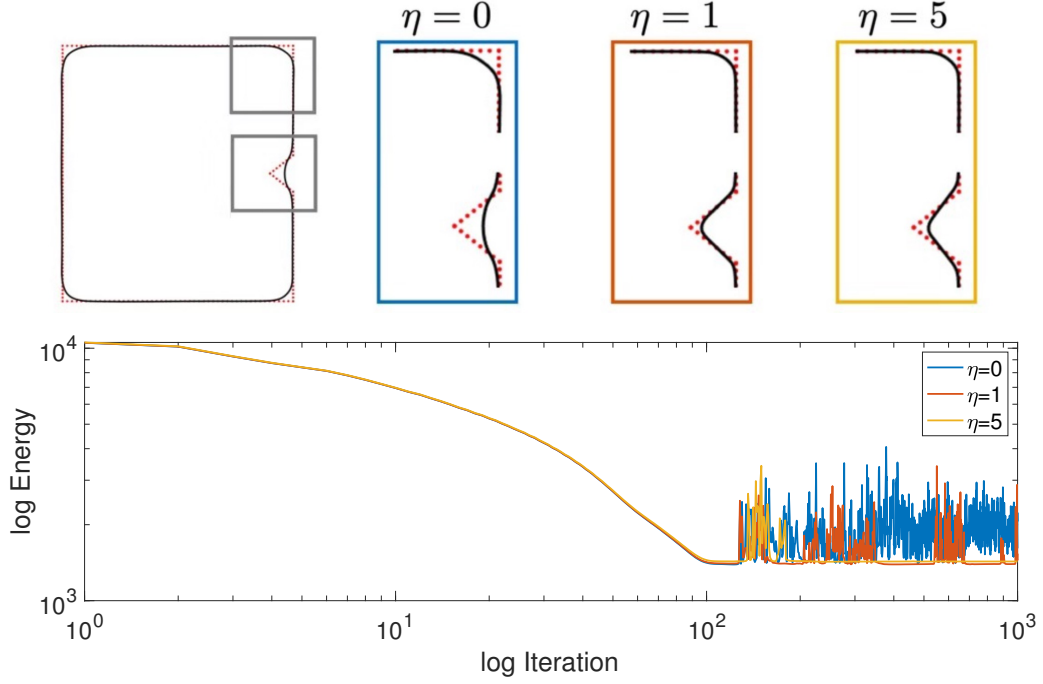


Figure 3: Effect of  $\eta$  in ALM. Here  $r_1 = 15$ ,  $r_2 = 10$ , and  $r_3 = 3$  are fixed. Increasing  $\eta$  induces reconstruction of the concave wedge. Although in cases, the energy curves are identical before the 100-th step, larger  $\eta$  suppresses the oscillation of the energy curve: yellow line ( $\eta = 5$ ) is more stable compared to red ( $\eta = 1$ ) or blue ( $\eta = 0$ ).

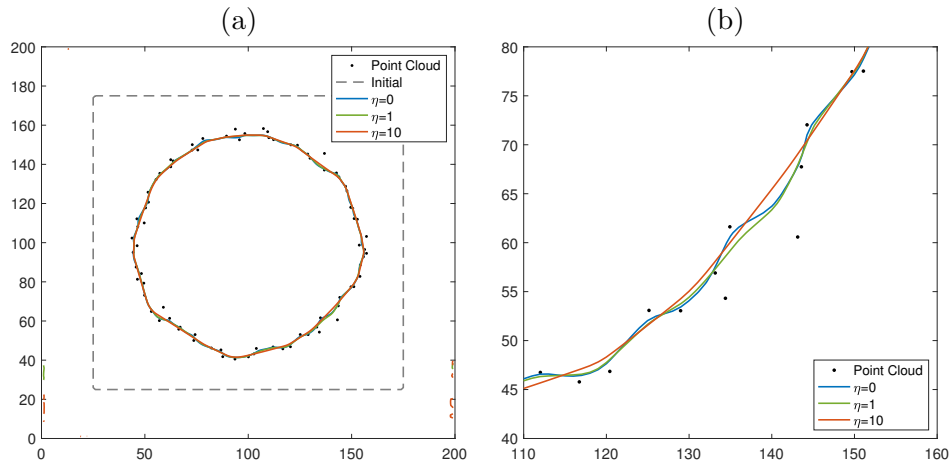


Figure 4: ALM with noisy data and  $r_1 = 15$ ,  $r_2 = 10$ ,  $r_3 = 3$ . The noise is Gaussian noise with standard deviation 2. As  $\eta$  increases, the curve becomes less oscillatory.

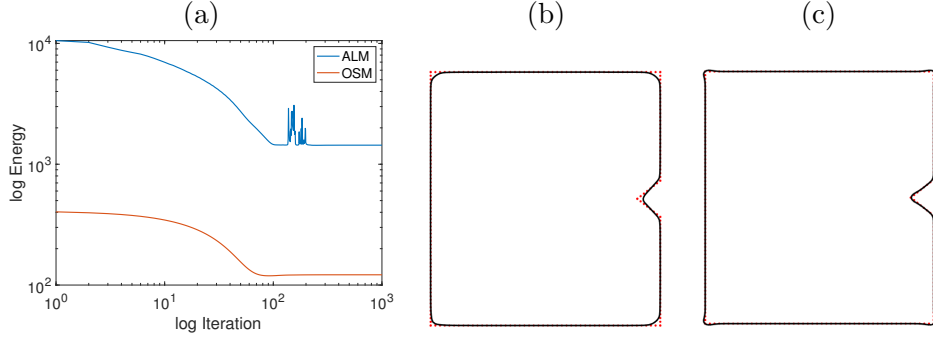


Figure 5: With  $\eta = 2$ , comparison between OSM and ALM. In ALM,  $r_1 = 15, r_2 = 10, r_3 = 3$  is used. Convergence to the steady state is faster for OSM. The reconstructed curves are shown in (b) for ALM and in (c) for OSM: ALM smooths out the corners, while OSM performs better in preserving corners.

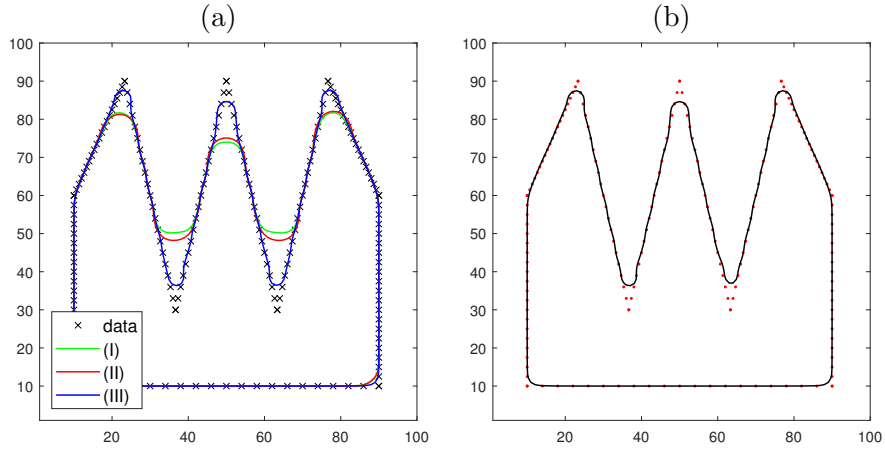


Figure 6: (a) By OSM with  $s = 2$  for the distance term in (2), the comparison between (I)  $\eta = 0$  (green curve), (II)  $s = 1$  (red curve), and (III)  $s = 2$  (blue curve) for the curvature term. (b) OSM with  $\eta = 2.5$  for  $s = 2$  in the model (5). This is the blue curve in (a). OSM using  $s = 2$  gives the best results capturing the structure of the underlying surface more accurately.

### 3.2 Comparison of OSM and ALM

Figure 5(a) shows the energy convergence comparison between OSM (with  $s = 2$ ) and ALM ( $s = 1$ ). In ALM,  $r_1 = 15, r_2 = 10, r_3 = 3$  is used. Convergence to the steady state is faster for OSM. The reconstructed curves are shown in Figure 5(b) and (c). ALM prefers to smooth out the corners. Operator splitting method performs better in preserving corners, while the results extrudes out a little bit at all corners.

Using OSM, we fix  $s = 2$  for the distance term in (2) and explore the difference between using (I) no curvature term  $\eta = 0$ , (II)  $l_1$  of the mean curvature term with  $s = 1$ , and (III)  $l_2$  of the mean curvature term  $s = 2$ . Figure 6 (a) shows the comparison between  $\eta = 0$  (green curve),  $s = 1$  (red curve), and  $s = 2$  (blue curve). The blue curve (OSM with  $s = 2$ ) in (a) is presented separately in Figure 6 (b). OSM using  $s = 2$  gives the best result capturing the structure of the underlying surface more accurately. The rest of the numerical experiments use operator splitting, which gives more stable results with less number of parameters and faster convergence with smaller energy minimization.

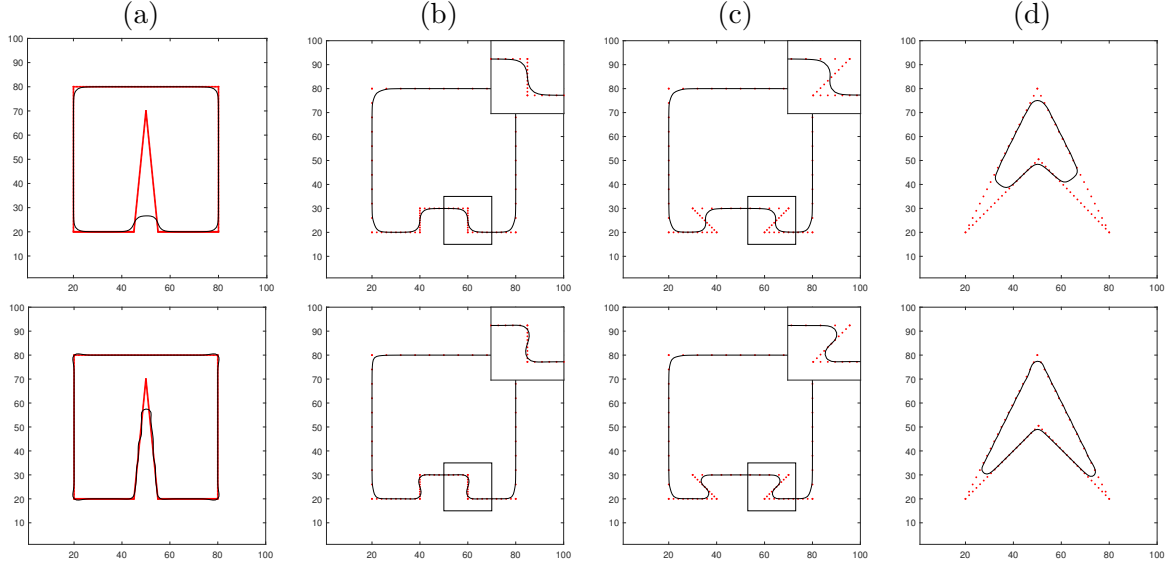


Figure 7: By OSM, comparison with or without curvature constraints: The top row results are without any curvature term,  $\eta = 0$ , and the second row results are with curvature constraint ( $s = 2$ ): (a)  $\eta = 3$ , (b)  $\eta = 2$ , (c)  $\eta = 1$ , and (d)  $\eta = 2$ . The shape of the underlying surface are more accurately captured using the curvature constraint.

### 3.3 Effect of curvature constraint: OSM with $s = 2$

Figure 7 shows the comparison between  $\eta = 0$  (top row) and  $\eta \neq 0$  (the second row). With the curvature term, the shape of the underlying surface is much better captured in the second row. In the interior triangle shape of Figure 7(a) is better captured with the curvature term. Without the curvature term, the reconstructed curve won't move further inside, since the prominent part has attained the balance between the curves length and its distance to the two edges of the triangle. Notice that the prominent part in the top row is not flat, and its curvature is non-zero. With a positive  $\eta$ , this balance is broken and the prominent part will further move towards the upper vertex of the triangle. Also, for the cases with sharp corners Figure 7(c)-(d), our method improves the results and recover the underlying shape better.

As  $\eta$  increases, different effect can be shown, e.g., Figure 8. As one increases  $\eta$ , the two sharp corners are recovered better. However, if  $\eta$  is too large, like 3 and 4 in this example, the corners gets more circular. As  $\eta$ , the weight of curvature term, gets larger the reconstructed curves becomes more circular to avoid large curvature.

Figure 9 shows results when the given point cloud are sparse, for a boomerang shape and a sparse square. With sparse boomerang data, just using distance term ( $\eta = 0$ ) can recover very limited part of the given point cloud, a small triangle, see Figure 9 (a). With  $\eta = 4$ , We recover the general shape of boomerang in Figure 9(b). For the sparse square shape, only four corners and one point in each sides are given in Figure 9(c)-(d). While for  $\eta = 0$ , the bottom part of recovered shape is smooth, with  $\eta = 2$ , the rectangle shape is recovered much clearly showing sharper corners in the bottom area in Figure 9(d). Figure 10 shows the case when even less number of points are given, see Figure 10(a). Only two points around each corners are given. Figure 10 (b) and (c) shows results with  $\eta = 1$  and  $\eta = 1.5$ , respectively. Even with extremely sparse data, curvature constraint model can reconstruct the square corners well.

Next experiment is for the noisy boomerang data, Gaussian noise with standard deviation 1 is added. The results with  $\eta = 0, 1, 2$  are shown in Figure 11. As  $\eta$  gets larger, the narrower parts gets recovered better. Even with noisy data, our operator splitting method can still reconstruct the sharp corners.

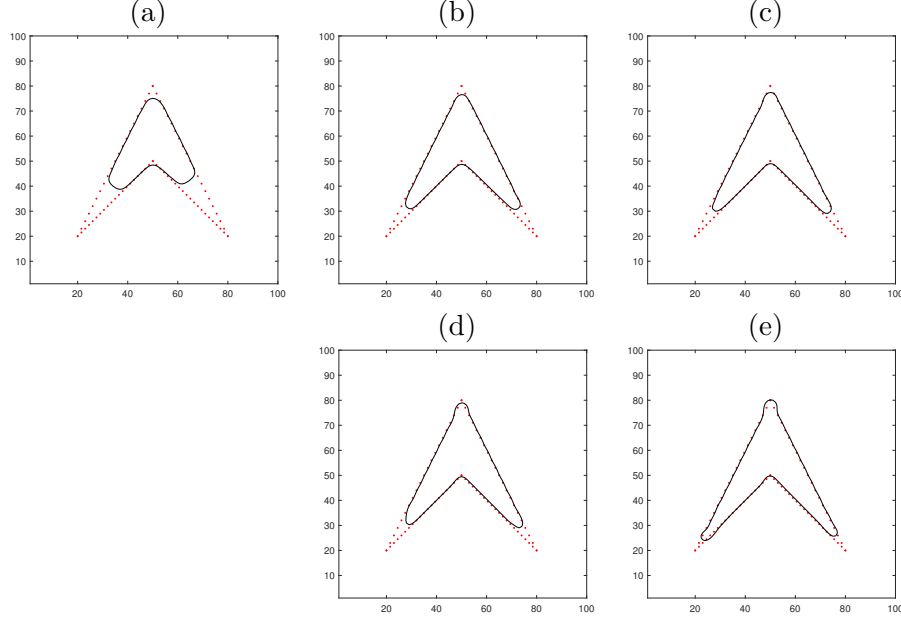


Figure 8: Effect of  $\eta$  in OSM. (a)  $\eta = 0$ . (b)  $\eta = 1$ . (c)  $\eta = 2$ . (d)  $\eta = 3$ . (e)  $\eta = 4$ . As  $\eta$  increases, the two sharp corners are recovered better. As  $\eta$  gets larger, more circular the corners gets to avoid large curvature.

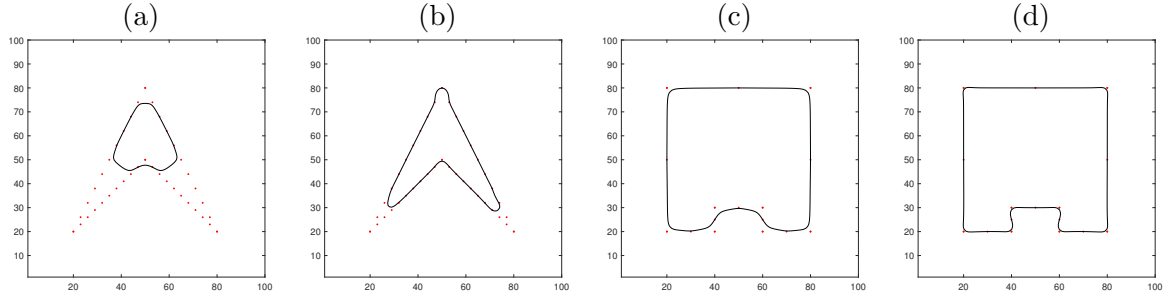


Figure 9: By OSM, sparse data results with or without curvature constraints: Using (a)  $\eta = 0$ , and (b)  $\eta = 4$  for a point cloud sampled from a Boomerang shape. Using (c)  $\eta = 0$  and (d)  $\eta = 2$ , for a sparse square shape where only four corners and one point in each sides are given. For both examples, with curvature constraint, the recovery is more accurate and sharper.

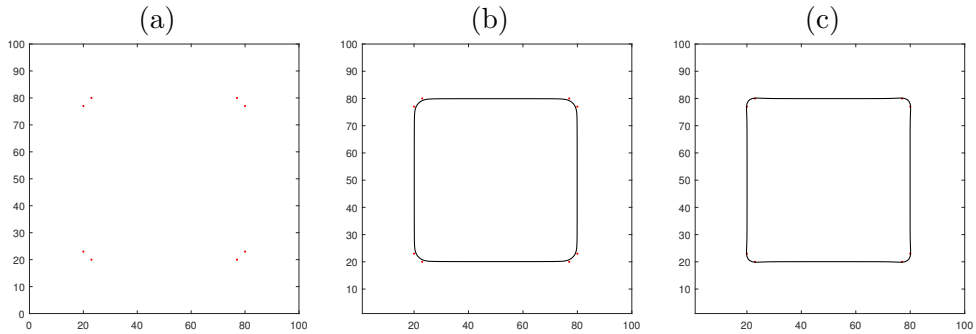


Figure 10: BY OSM, extremely sparse data: (a) Given data. (b) is the recovered result with  $\eta = 1$  and (c) with  $\eta = 1.5$ . Even with extremely sparse data, curvature constraint model can reconstruct the square corners well.

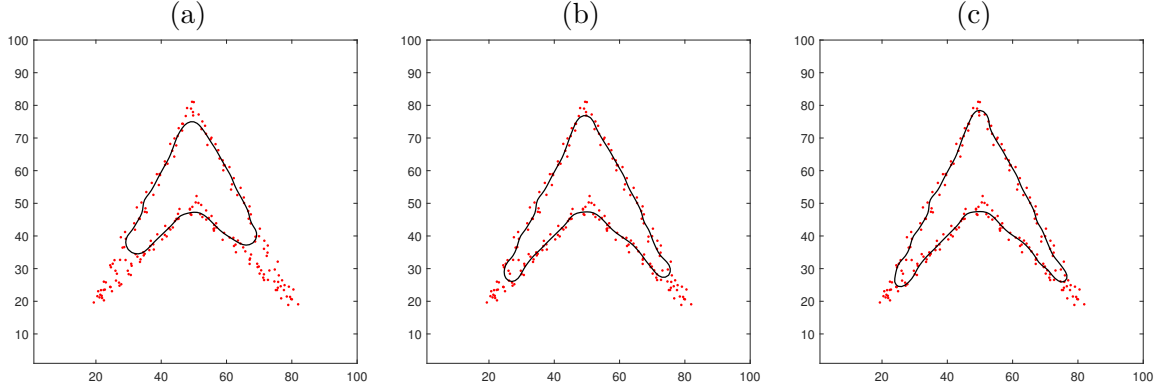


Figure 11: By OSM, reconstruction with noisy data: (a)  $\eta = 0$ , (b)  $\eta = 1$ , (c)  $\eta = 2$ . The noise is Gaussian noise with standard deviation 1. As  $\eta$  gets larger, the narrower parts gets recovered better.

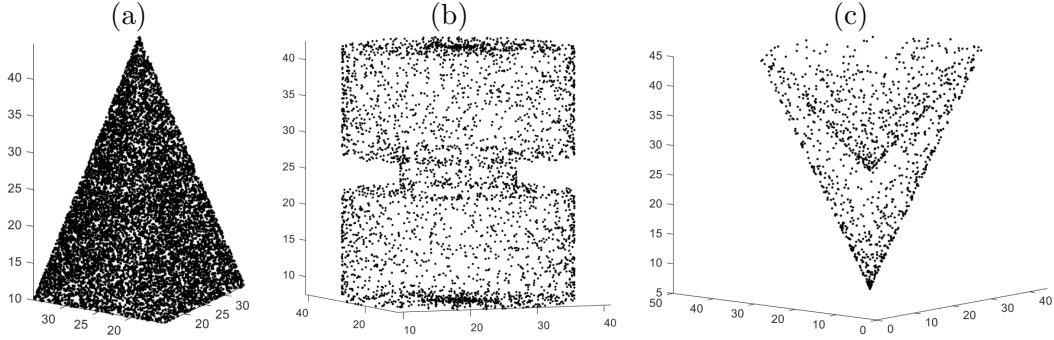


Figure 12: Given data of three dimensional examples: (a) A pyramid. (b) A yoyo. (c) An ice cream cone.

### 3.4 Three Dimensional Examples

We conclude this section by showing some reconstructed surfaces in three dimensional space. We use OSM to reconstruct the pyramid, yoyo and ice cream cone. The given data is shown in Figure 12. For the pyramid, we use  $\Delta t = 500$ . The reconstructed surface with  $\eta = 0, 5, 10$  and the comparison of cross sections along  $y = 25$  are shown in Figure 13. The effect of the curvature term is not significant, while we can see some improvements of capturing the vertices.

For the yoyo, we use  $\Delta t = 100$ . The reconstructed surface with  $\eta = 0, 5$  and the comparison of cross sections along  $y = 25$  are shown in Figure 14. The advantage of the curvature term is obvious. With  $\eta = 0$ , the solution attains the energy balance between surface area and distance to the data at some location away from the middle neck part. Since its curvature at that part is non-zero, given a positive  $\eta$ , the surface further evolves to capture the neck.

For the ice cream cone, we use  $\Delta t = 100$ . This is not a standard ice cream cone, that its surface consists of two layers. The cross section of the ice cream cone looks like a boomerang. For this example, if we use  $\eta = 0$ , the solution shrinks to a point and then disappears. The reconstructed surface with  $\eta = 5, 10$  and the comparison of cross sections along  $y = 25$  are shown in Figure 15. The effect of the value of  $\eta$  on this ice cream cone is similar to that on boomerang. Solution with larger  $\eta$  captures the sharp corner better.



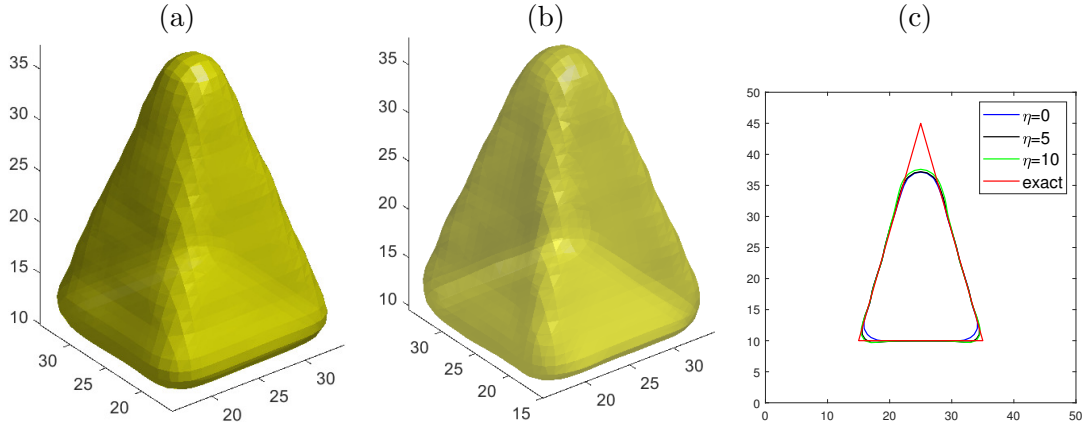


Figure 13: Reconstruct pyramid by OSM: (a) Result with  $\eta = 0$ . (b) Result with  $\eta = 10$ . (c) Comparison of cross section along  $y = 25$ .

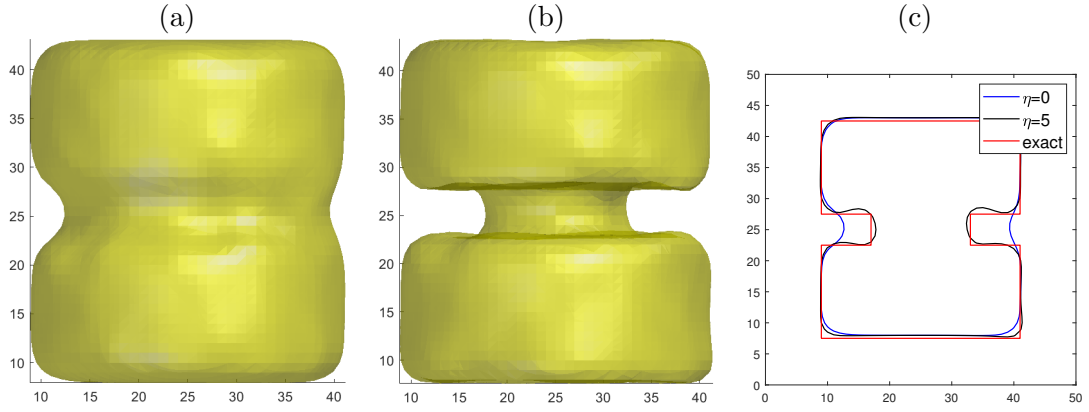


Figure 14: Reconstruction of yoyo by OSM: (a) Result with  $\eta = 0$ . (b) Result with  $\eta = 5$ . (c) Comparison of cross section along  $y = 25$ .

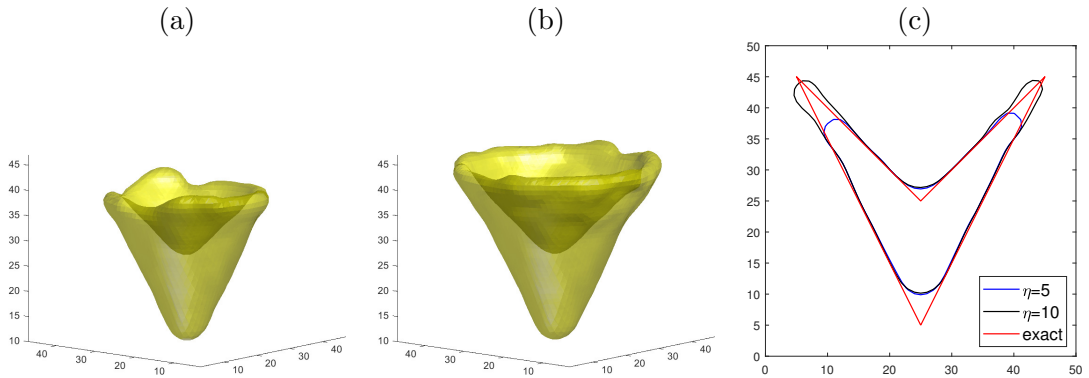


Figure 15: Reconstruction of ice cream cone by OSM: (a) Result with  $\eta = 5$ . (b) Result with  $\eta = 10$ . (c) Comparison of cross section along  $y = 25$ .

## 4 Analytical Aspects of the Model

We consider the first variation of each terms of the functional (2). First, the distance from surface to the point cloud,  $d$ , effects the shape of  $\Gamma$ . Denoting  $\mathbf{n}$  as the surface normal, the first variation of (2) when  $\eta = 0$  is [39]:

$$\frac{1}{s} \left( \int_{\Gamma} d^s(\mathbf{x}) d\sigma \right)^{1/s-1} (s d^{s-1} \nabla d \cdot \mathbf{n} + d^s \kappa), \quad (29)$$

which shows the interaction between the data-dependent driving force,  $d$ , and the shape determining factor,  $\kappa$ . When  $\Gamma$  is close to point cloud, i.e.,  $d$  is small, then the shape of  $\Gamma$  becomes flexible, i.e.,  $\kappa$  can be large; when  $\Gamma$  is away from the point cloud, i.e.,  $d$  is large, then the shape of  $\Gamma$  becomes rigid, and  $\kappa$  must be small. Second, the effect of the mean-curvature  $\kappa$  of  $\Gamma$  is adjusted by the surface area. Notice that this term only focuses on the geometry of  $\Gamma$ , and the point cloud data has no influence. The first variation of the functional  $(\int_{\Gamma} |\kappa(\mathbf{x})|^s d\sigma)^{1/s}$  can be derived [6]:

$$\frac{1}{s} \left( \int_{\Gamma} |\kappa(\mathbf{x})|^s d\sigma \right)^{1/s-1} \times \begin{cases} \text{div}_{\Gamma}(\delta(\kappa) \nabla_{\Gamma} \kappa) + |\kappa| \kappa^{-1} |W|^2 - \kappa |\kappa| & s = 1 \\ -\text{div}_{\Gamma}(|\kappa|^s \kappa^{-3} (s(s-2) - s\kappa) \nabla_{\Gamma} \kappa) + s |\kappa|^s \kappa^{-1} |W|^2 - \kappa |\kappa|^s & s \geq 2. \end{cases} \quad (30)$$

Here  $\nabla_{\Gamma}$  is the tangent component of the gradient, and  $\text{div}_{\Gamma}$  is its dual operator;  $W$  is the Weingarten map of  $\Gamma$ , and  $|W|^2$  equals the squared Gaussian curvature if  $\Gamma$  is a 2D surface. Compared to (29), the first variation related to the regularization term (30) is more complicated. There are no strong relation can be reduces, other than the fact that while the term (29) connects the distance and curvature, this term (30) only depends on  $\kappa$ .

When  $s = 1$  in the model (2), we compare the cases with  $\eta = 0$  and  $\eta \neq 0$ . The minimizer has a constant-mean-curvature  $\kappa \neq 0$ , since there is no compact minimal surface. When  $\eta = 0$  without the curvature constraint, a minimizer of (2) satisfies the necessary condition  $\nabla d \cdot \mathbf{n} + d\kappa = \nabla \cdot (d\mathbf{n}) = 0$ ; when  $\eta \neq 0$  with the curvature constraint, the equation becomes  $\nabla d \cdot \mathbf{n} + (d + \eta |\kappa|^{-1} |W|^2 - \eta |\kappa|) \kappa = \nabla \cdot ((d - \eta |\kappa| \kappa) \mathbf{n}) + \eta \text{sign}(\kappa) |W|^2 = 0$ . With the curvature constraint, the model modifies the effect of the function  $d$  by considering both the value and the sign of  $\kappa$ . In addition, the equation becomes inhomogeneous with a forcing term closely related to the local concavity/convexity and the Gaussian curvature. These modifications introduce more complexity into the model behavior, and our experiments show that they can help to improve reconstruction results.

When  $s = 2$ , the first variation of the curvature regularization term  $(\int_{\Gamma} \kappa^2 d\sigma)^{1/2}$  becomes:

$$\left( \int_{\Gamma} \kappa(\mathbf{x})^2 d\sigma \right)^{-1/2} (\Delta_{\Gamma} \kappa + \kappa G^2 - \kappa^3/2), \quad (31)$$

where  $\Delta_{\Gamma}$  is the Laplace-Beltrami operator, and  $G$  is the Gaussian curvature. Since (31) contains  $\Delta_{\Gamma} \kappa$ , we expect to see that our model with  $s = 2$  will be influenced by the locally averaged mean curvature, which leads to smoothing effects. Here we show this model's behavior in the following special case.

**Proposition 4.1.** *Suppose the point cloud is sampled from a smooth closed surface  $\Gamma$  with mean curvature  $\kappa$  and Gaussian curvature  $G$  satisfying:*

$$\kappa(G^2 - \kappa^2/2) = 0. \quad (32)$$

*If the point cloud is sufficiently dense, i.e. the computed  $d$  is very close to the exact distance function, then  $\Gamma$  is a minimizer of (2) only if it is a sphere of radius  $1/\sqrt{2}$ .*

*Proof.* Since  $\Gamma$  passes through the point cloud, (29) degenerates to 0. Moreover, by (32) together with (30), the necessary condition for  $\Gamma$  being a minimizer is that  $\Delta_\Gamma \kappa = 0$ . Because  $\Gamma$  is closed,  $\kappa$  is a non-zero constant. By (32), this implies that  $G$  is also constant; hence, we know that  $\Gamma$  can only be a sphere. Finally, since  $G = 1/r^2$  and  $\kappa = -2/r$  with  $r$  the radius of the sphere, we can solve for the radius of  $\Gamma$ , which is  $1/\sqrt{2}$ .  $\square$

The curvature regularization term  $(\int_\Gamma \kappa^2 d\sigma)^{1/2}$  inflates the membrane supported by the point cloud. Mylar balloon [22], which resembles slightly flattened sphere, satisfies the condition (32). Proposition 4.1 claims that, if the point cloud lies on a Mylar balloon, the minimizers of the functional (2) are not the underlying surfaces.

The following shows a two dimensional example in which the object is a circle, denoted by  $C_0$ , centered at the origin with radius  $r_0$ . It is fair to assume that a local minimizer of  $E_s(\Gamma)$  is a circle, denoted by  $C$ , with the same center and radius close to  $r_0$ . Denote the radius of  $C$  by  $r$ . Then we have the following proposition:

**Proposition 4.2.** *Under the setting of the above example, for  $s = 1$ ,  $r = r_0$  is a local minimizer of  $E_1(C)$  for any  $\eta$ . For  $s = 2$ ,  $r = r_0$  is a local minimizer of  $E_2(C)$  if  $\eta \leq 2r_0$  and  $r = (r_0 + \sqrt{r_0^2 + 12\eta})/6$  is a local minimizer if  $\eta > 2r_0$ .*

*Proof.* Note that for a circle with radius  $r$  and the same center as  $C_0$ ,  $d = |r - r_0|$  and  $\kappa = 1/r$ .  $E_s(C)$  can be written as

$$E_s(C) = (2\pi)^{\frac{1}{s}} \left( |r - r_0| r^{\frac{1}{s}} + \eta r^{\frac{1}{s}-1} \right).$$

For  $s = 1$ ,  $E_1(C) = (2\pi)^{\frac{1}{s}} \left( |r - r_0| r^{\frac{1}{s}} + \eta \right)$  of which  $C_0$  is a local minimizer for any  $\eta$ .

For  $s = 2$ ,  $E_2(C) = (2\pi)^{\frac{1}{2}} \left( |r - r_0| r^{\frac{1}{2}} + \eta r^{-\frac{1}{2}} \right)$  whose subdifferential is

$$\partial E_2(C) = \begin{cases} (2\pi)^{\frac{1}{2}} \left( \frac{r_0}{2} r^{-\frac{1}{2}} - \frac{3}{2} r^{\frac{1}{2}} - \frac{\eta}{2} r^{-\frac{3}{2}} \right), & \text{for } r < r_0, \\ (2\pi)^{\frac{1}{2}} \left( \frac{3}{2} r^{\frac{1}{2}} - \frac{r_0}{2} r^{-\frac{1}{2}} - \frac{\eta}{2} r^{-\frac{3}{2}} \right), & \text{for } r > r_0. \end{cases}$$

For  $r < r_0$ , it can be easily shown that if  $12\eta \leq r_0^2$  and  $(r_0 + \sqrt{r_0^2 - 12\eta})/6 < r < r_0$ ,  $\partial E_2(C) < 0$ . If  $12\eta > r_0^2$ ,  $\partial E_2(C) < 0$  for any  $r < r_0$ . In other words, if  $r < r_0$  and  $r$  is sufficiently close to  $r_0$ ,  $\partial E_2(C) < 0$ .

For  $r > r_0$ , if  $\eta \leq 2r_0$ ,  $\partial E_2(C) > 0$  and thus  $r = r_0$  is a local minimizer of  $E_2(C)$ . If  $\eta > 2r_0$ , then  $\partial E_2(C) < 0$  for  $r_0 < r < (r_0 + \sqrt{r_0^2 + 12\eta})/6$  and  $\partial E_2(C) > 0$  for  $r > (r_0 + \sqrt{r_0^2 + 12\eta})/6$ . Thus  $r = (r_0 + \sqrt{r_0^2 + 12\eta})/6$  is a local minimizer of  $E_2(C)$ .  $\square$

These properties show that the minimizer of the model (2) is not easy to be analyzed even in a simple cases like circle, and the results are heavily depended on the combination of  $d$  and  $\kappa$ .

## 5 Conclusion

In this paper, we explore the surface reconstruction models from point cloud data with curvature constraints. The model combines the distance from surface to point cloud with a global curvature regularization. Introducing this high-order geometric information allows us to impose geometric features around the corners and to reconstruct concave parts of the underlying shapes better. To avoid the complicated terms in the Euler-Lagrange equations of the proposed functional, we take a new operator splitting strategy and minimizes the energy by a semi-implicit scheme. We also explore an augmented Lagrangian method, which has the advantages of less parameters compared to other ADMM approaches. Both methods are computationally efficient

and produce reliable results in many cases, including those where the point cloud is noisy or sparse. Comparison between OSM and ALM shows advances of OSM for the case with  $s = 1$ . Among using  $\eta = 1$ ,  $s = 1$  and  $s = 2$  for OSM, using  $s = 2$  shows the most stable result with fast computation.

## Acknowledgment

The authors would like to thank Dr. Martin Huska at University of Bologna, Italy for the valuable discussions exploring different approaches of fast algorithm for high order functionals.

## References

- [1] E. Bae, X.-C. Tai, and W. Zhu. Augmented Lagrangian method for an Euler’s elastica based segmentation model that promotes convex contours. *Inverse Problems & Imaging*, 11(1):1–23, 2017.
- [2] W. Blaschke. Über topologische fragen der differentialgeometrie. *Jahresbericht der Deutschen Mathematiker-Vereinigung*, 38:193–205, 1929.
- [3] K. Bredies, T. Pock, and B. Wirth. A convex, lower semicontinuous approximation of Euler’s elastica energy. *SIAM Journal on Mathematical Analysis*, 47(1):566–613, 2015.
- [4] C. Brito-Loeza and K. Chen. Multigrid method for a modified curvature driven diffusion model for image inpainting. *Journal of Computational Mathematics*, pages 856–875, 2008.
- [5] L.-J. Deng, R. Glowinski, and X.-C. Tai. A new operator splitting method for the Euler elastica model for image smoothing. *SIAM Journal on Imaging Sciences*, 2019.
- [6] M. Droske and A. Bertozzi. Higher-order feature-preserving geometric regularization. *SIAM Journal on Imaging Sciences*, 3(1):21–51, 2010.
- [7] V. Estellers, D. Zosso, R. Lai, S. Osher, J.-P. Thiran, and X. Bresson. Efficient algorithm for level set method preserving distance function. *IEEE Transactions on Image Processing*, 21(12):4722–4734, 2012.
- [8] R. Glowinski and P. Le Tallec. *Augmented Lagrangian and Operator-Splitting Methods in Nonlinear Mechanics*, volume 9. SIAM, 1989.
- [9] R. Glowinski, S. J. Osher, and W. Yin. *Splitting Methods in Communication, Imaging, Science, and Engineering*. Springer, 2017.
- [10] B. Goldluecke and D. Cremers. Introducing total curvature for image processing. In *2011 International Conference on Computer Vision*, pages 1267–1274. IEEE, 2011.
- [11] L. Gomes, O. R. P. Bellon, and L. Silva. 3D reconstruction methods for digital preservation of cultural heritage: A survey. *Pattern Recognition Letters*, 50:3–14, 2014.
- [12] Y. Gong and O. Goksel. Weighted mean curvature. *Signal Processing*, 164:329 – 339, 2019.
- [13] Y. Gong and I. F. Sbalzarini. Local weighted gaussian curvature for image processing. In *2013 IEEE International Conference on Image Processing*, pages 534–538. IEEE, 2013.
- [14] J. Haličková and K. Mikula. Level set method for surface reconstruction and its application in surveying. *Journal of Surveying Engineering*, 142(3):04016007, 2016.

- [15] C. Y. Kao, S. Osher, and J. Qian. Lax–Friedrichs sweeping scheme for static Hamilton–Jacobi equations. *Journal of Computational Physics*, 196(1):367–391, 2004.
- [16] D. Khan, M. A. Shirazi, and M. Y. Kim. Single shot laser speckle based 3D acquisition system for medical applications. *Optics and Lasers in Engineering*, 105:43–53, 2018.
- [17] H. Li, Y. Li, R. Yu, J. Sun, and J. Kim. Surface reconstruction from unorganized points with  $\ell_0$  gradient minimization. *Computer Vision and Image Understanding*, 169:108–118, 2018.
- [18] J. Liang, F. Park, and H.-K. Zhao. Robust and efficient implicit surface reconstruction for point clouds based on convexified image segmentation. *Journal of Scientific Computing*, 54(2-3):577–602, 2013.
- [19] H. Liu, X. Wang, and W. Qiang. Implicit surface reconstruction from 3D scattered points based on variational level set method. In *2008 2nd International Symposium on Systems and Control in Aerospace and Astronautics*, pages 1–5. IEEE, 2008.
- [20] H. Liu, Z. Yao, S. Leung, and T. F. Chan. A level set based variational principal flow method for nonparametric dimension reduction on Riemannian manifolds. *SIAM Journal on Scientific Computing*, 39(4):A1616–A1646, 2017.
- [21] L. M. Lui, C. Wen, and X. Gu. A conformal approach for surface inpainting. *Inverse Problems and Imaging*, 7(3):863–884, 2013.
- [22] I. M. Mladenov and J. Oprea. The mylar ballon: New viewpoints and generalizations. In *Proceedings of the Eighth International Conference on Geometry, Integrability and Quantization*, pages 246–263. Institute of Biophysics and Biomedical Engineering, Bulgarian Academy of Sciences, 2007.
- [23] S. Osher, R. Fedkiw, and K. Piechor. Level set methods and dynamic implicit surfaces. *Appl. Mech. Rev.*, 57(3):B15–B15, 2004.
- [24] S. Osher and J. A. Sethian. Fronts propagating with curvature-dependent speed: algorithms based on Hamilton–Jacobi formulations. *Journal of Computational Physics*, 79(1):12–49, 1988.
- [25] X. Qiao. The principle curvature-driven diffusion model for image de-noising. In *3rd International Conference on Multimedia Technology (ICMT-13)*. Atlantis Press, 2013.
- [26] T. Schoenemann, F. Kahl, S. Masnou, and D. Cremers. A linear framework for region-based image segmentation and inpainting involving curvature penalization. *International Journal of Computer Vision*, 99(1):53–68, 2012.
- [27] T. Schoenemann, S. Masnou, and D. Cremers. The elastic ratio: Introducing curvature into ratio-based image segmentation. *IEEE Transactions on Image Processing*, 20(9):2565–2581, 2011.
- [28] J. Shen, S. H. Kang, and T. F. Chan. Euler’s elastica and curvature-based inpainting. *SIAM Journal on Applied Mathematics*, 63(2):564–592, 2003.
- [29] J. Shi, M. Wan, X.-C. Tai, and D. Wang. Curvature minimization for surface reconstruction with features. In *International Conference on Scale Space and Variational Methods in Computer Vision*, pages 495–507. Springer, 2011.
- [30] Y. Shi and W. C. Karl. Shape reconstruction from unorganized points with a data-driven level set method. In *2004 IEEE International Conference on Acoustics, Speech, and Signal Processing*, volume 3, pages iii–13. IEEE, 2004.

- [31] P. Smereka. Semi-implicit level set methods for curvature and surface diffusion motion. *Journal of Scientific Computing*, 19(1):439–456, 2003.
- [32] X.-C. Tai, J. Hahn, and G. J. Chung. A fast algorithm for Euler’s elastica model using augmented Lagrangian method. *SIAM Journal on Imaging Sciences*, 4(1):313–344, 2011.
- [33] X.-C. Tai and C. Wu. Augmented lagrangian method, dual methods and split bregman iteration for rof model. In *International Conference on Scale Space and Variational Methods in Computer Vision*, pages 502–513. Springer, 2009.
- [34] H. F. Trotter. On the product of semi-groups of operators. *Proceedings of the American Mathematical Society*, 10(4):545–551, 1959.
- [35] T. Willmore. Mean curvature of immersed surfaces. *An. Sti. Univ. Al. I. Cuza Iasi, Sec. I. a Mat.(NS)*, 14:99–103, 1968.
- [36] F. Yang, K. Chen, and B. Yu. Homotopy method for a mean curvature-based denoising model. *Applied Numerical Mathematics*, 62(3):185–200, 2012.
- [37] M. Yashtini and S. H. Kang. A fast relaxed normal two split method and an effective weighted tv approach for euler’s elastica image inpainting. *SIAM Journal on Imaging Sciences*, 9(4):1552–1581, 2016.
- [38] H.-K. Zhao, S. Osher, and R. Fedkiw. Fast surface reconstruction using the level set method. In *Proceedings IEEE Workshop on Variational and Level Set Methods in Computer Vision*, pages 194–201. IEEE, 2001.
- [39] H.-K. Zhao, S. Osher, B. Merriman, and M. Kang. Implicit and nonparametric shape reconstruction from unorganized data using a variational level set method. *Computer Vision and Image Understanding*, 80(3):295–314, 2000.
- [40] W. Zhu and T. Chan. Image denoising using mean curvature of image surface. *SIAM Journal on Imaging Sciences*, 5(1):1–32, 2012.
- [41] W. Zhu, X.-C. Tai, and T. Chan. Image segmentation using Euler’s elastica as the regularization. *Journal of Scientific Computing*, 57(2):414–438, 2013.